



Mechanical characteristics under monotonic and cyclic simple shear of spark plasma sintered ultrafine-grained nickel

G. Dirras^{a,*}, S. Bouvier^a, J. Gubicza^b, B. Hasni^a, T. Szilágyi^b

^a LPMTM – CNRS, Institut Galilée, Université Paris 13, 99 Avenue J.B. Clément, 93430 Villetaneuse, France

^b Department of Materials Physics, Eötvös Loránd University, P.O.B. 32, Budapest H-1518, Hungary

ARTICLE INFO

Article history:

Received 23 April 2009

Received in revised form 11 July 2009

Accepted 17 July 2009

Keywords:

Nickel

Powder consolidation

Ultrafine-grained microstructure

Simple shear test

Twin grain boundary

ABSTRACT

The present work focuses on understanding the mechanical behavior of bulk ultrafine-grained nickel specimens processed by spark plasma sintering of high purity nickel nanopowder and subsequently deformed under large amplitude monotonic simple shear tests and strain-controlled cyclic simple shear tests at room temperature. During cyclic tests, the samples were deformed up to an accumulated von Mises strain of about $\varepsilon_{VM} = 0.75$ (the flow stress was in the 650–700 MPa range), which is extremely high in comparison with the low tensile/compression ductility of this class of materials at quasi-static conditions. The underlying physical mechanisms were investigated by electron microscopy and X-ray diffraction profile analysis. Lattice dislocation-based plasticity leading to cell formation and dislocation interactions with twin boundaries contributed to the work-hardening of these materials. The large amount of plastic strain that has been reached during the shear tests highlights intrinsic mechanical characteristics of the ultrafine-grained nickel studied here.

© 2009 Elsevier B.V. All rights reserved.

1. Introduction

Ultrafine-grained (*ufg*) metals and alloys are materials having grain sizes (*d*) in the 100 nm–1 μ m range and exhibit a high room temperature (RT) yield strength [1,2] compared to conventional materials with large grains in accordance with the Hall–Petch (HP) relationship [3,4]. Unfortunately as shown by the body of the existing literature data [5–8] the observed high yield strength is usually accompanied by a lack of tensile ductility during monotonic testing of these materials, especially within the lower grain size range of *ufg* materials. This is particularly true for powder metallurgy (PM) processed materials because of processing defects such as impurities or incomplete particle bonding. Despite the processing of specific microstructures such as nanotwinned Co [9] or Cu [10] processed by electrodeposition that exhibit an appreciable tensile ductility at RT, studies reporting on the deformation mechanisms of *ufg* polycrystals at finite strains are scarce. This paucity therefore limits the use of this promising class of materials despite strategies that have been suggested to increase their ductility [11].

Cyclic loadings are of particular interest for many structural applications. Limited studies have been conducted on *ufg* Al [12,13], Ti [14] and Cu [15,16], mostly processed by equal channel angular pressing because of its capability to produce contaminants and porosity-free *ufg* materials in bulk form. In majority, these studies

concerned with small amplitude strain- or stress-controlled tests in both low-cycle and high-cycle fatigue regime and valuable data have been gathered. For instance, in the case of *ufg* Al, it has been shown that the number of cycles to failure of the as-processed and annealed samples was far below that of the coarse-grained (*cg*) counterpart [12]. In addition the stress–strain curve showed energy dissipation that occurred in the course of straining, which is never observed for the *cg* material counterpart [12]. For ECAP-processed Ti, no cyclic softening or degradation during the strain-controlled experiments was noticed opposed to what was reported for wavy slip materials such as Cu [16]. Furthermore, rapid cyclic instability, severe damage localization and premature fatigue failure were reported whose origin was related to the microstructure instability of the ECAP-processed *ufg* metals [15]. In the same context, the Bauschinger effect during uniaxial loading and unloading of *ufg* Cu has been investigated [14,17]. The influence of the heat treatment on the saturation stress, the hardening evolution and tensile–compression asymmetry, have been reported.

Nickel is one of the most studied metallic materials and an abundant experimental and theoretical literature exists on the deformation mechanisms of nanocrystalline (*nc*) and *ufg* Ni processed by different routes and deformed via various mechanical tests in the quasi-static strain rate regime at RT [18–25]. In addition, *ufg* nickel is a promising material for applications in such a field as micro-electro mechanical systems (MEMS) [24,26,27], for which cyclic properties can be considered as key issues. Therefore, for reliability matter, it is important to analyze mechanical properties versus microstructure relationships of *ufg* microstructures

* Corresponding author. Tel.: +33 1 49 40 34 88; fax: +33 1 49 40 39 38.
E-mail address: dirras@univ-paris13.fr (G. Dirras).

by examining the material behavior at finite strain. Indeed, to the best of the authors' knowledge, no study reporting on the mechanical behavior and the underlying deformation mechanisms under large amplitude deformation-controlled monotonic simple shear, nor on large amplitude deformation-controlled cyclic simple shear has been conducted on this material, especially in the *ufg* regime. Contrariwise to microstructures processed by severe plastic deformation (SPD) and in spite of some inherent drawbacks, powder metallurgy routes yield stable and texture free bulk *ufg* specimens [1,28]. Nonetheless, as it is the case of the majority of *ufg* materials, it has been shown that the RT ductility of the microstructure from this type of process is low [1,2,29].

In the present work we report on the mechanical behavior and the underlying deformation mechanisms during large amplitude strain-controlled monotonous and cyclic simple shear tests at RT of *ufg* nickel specimens processed by spark plasma sintering (SPS).

2. Experimental procedures

High purity (99.99%) Ni nanopowder with a nominal particle size of 100 nm was supplied by Argonide Corporation (USA). The powder was produced by electro-explosion of Ni wires [30,31]. The bulk samples were processed by spark plasma sintering (SPS) route using a Sumitomo 3rd generation apparatus, located at the CNRS platform facility at CIRIMAT (Toulouse). The principles of SPS have been reported elsewhere [32]. Before SPS-processing, the capsule containing the powder was broken in air and rapidly transferred to the graphite mould. The powder was held under a pressure of 150 MPa at 500 °C for 4 min (sample A) and 2 min (sample B) while pulses of high current density were applied to the sample for promoting consolidation. After SPS, disks of 50 mm in diameter and ~3.15 mm (sample A) and ~2.85 mm (sample B) in thickness were obtained.

After processing, the densities of the as-processed bulk samples were determined by the Archimedes method [1]. The computed relative densities of the samples were $95.5 \pm 0.1\%$ and $97 \pm 0.1\%$ for samples A and B, respectively. Given that both samples have been processed under the same conditions (except for the duration of the SPS experiment), the observed difference of the relative densities between the two samples is partially due to the efficiency of the sintering process relative to the amount of powder as the amount of powder for the processing of sample B was lower (therefore less initial porosity) than that of sample A. In addition, the slightly higher amount of face centered cubic NiO phase (having lower density, 6.67 g/cm^3 , than that of Ni) in sample A revealed by X-ray diffraction investigation as described below may also contribute to the lower relative density of sample A.

The phase contents were further studied by X-ray diffraction (XRD) using a Philips Xpert powder diffractometer with $\text{CuK}\alpha$ radiation [28]. Further, the microstructure of the consolidated and the deformed samples was studied by X-ray line profile analysis using $\text{CoK}\alpha_1$ radiation. The scattered X-rays were detected by imaging plates with the angular resolution of 0.005° in Θ , where Θ is the angle of diffraction. The line profiles of Ni phase were evaluated using the extended Convolutional Multiple Whole Profile (eCMWP) fitting procedure as described in detail elsewhere [33,34]. This method gives the crystallite size, dislocation density (ρ) and the twin-fault probability (β) with good statistics. The twin-fault probability is defined as the fraction of the faulted $\{111\}$ planes along their normal vector. To complement XRD investigations, the microstructure of the bulk samples was also investigated by electron backscatter diffraction (EBSD) on a Leo S340 scanning electron microscope (SEM) and by transmission electron microscopy (TEM) using a JEOL-2011 electron microscope at an operating voltage of 200 kV. Before EBSD analysis, samples were electropolished with

A2 electropolishing solution from Struers at a voltage of 12 V for 15 s. EBSD analyses were carried out using a step size of $0.2 \mu\text{m}$. Specimens for TEM investigations were first thinned mechanically and dimpled to about $20 \mu\text{m}$ and followed by final thinning using a Gatan Precision Ion Polishing System (PIPS) until perforation. More details regarding the experimental procedure have been given elsewhere [28].

The mechanical behavior of the sintered samples was studied by monotonic, cyclic load/unload, Bauschinger simple and cyclic Bauschinger simple shear tests, conducted at RT. These tests were carried out by means of a shear device mounted on a MTS M20 testing machine bearing a maximum load capacity of 100 kN. The simple shear specimens were rectangular plates of 30 mm length and 18 mm width cut through the thickness of the disks by electro discharge machining (EDM) to avoid surface hardening. Fig. 1a and b shows the location of the specimens in the compacted disks used in different mechanical tests. Specimens A1–A3 were subjected to monotonic simple shear test, while samples A4, A5 and A6 were used in cyclic Bauschinger simple shear test, simple shear load/unload test and Bauschinger simple shear test, respectively. Specimens B1, B2, B3 and B4 were subjected to Bauschinger simple shear, monotonic simple shear, cyclic Bauschinger simple shear and simple shear load/unload tests, respectively. Standard mechanical polishing using SiC papers and diamond paste was conducted in order to (i) remove the surface layer which might be remelted due to EDM and (ii) achieve a smooth surface free from stripes to reduce crack initiation during mechanical tests. The gauge area is limited to $30 \text{ mm} \times 2 \text{ mm}$. The final sample thickness was about 1 mm. It is worth noticing that the samples taken from the mid-thickness of the compacted disks displayed some porosity that was revealed after polishing, particularly for sample A. The planar simple shear test device consists of two rigid bodies, one of which is subjected to a translational movement relative to the other. The specimens were firmly fixed on the two bodies by two pairs of grips. A sketch of the shear device and specimen clamping is shown in Fig. 1c. All simple shear tests were performed using a constant plastic shear rate $1.732 \times 10^{-3} \text{ s}^{-1}$ (which corresponds to an equivalent von Mises strain rate of 10^{-3} s^{-1}). More details about the simple shear tests have been given elsewhere [35,36].

3. Results

3.1. Microstructure characteristics of the as-processed samples

The characteristics of the microstructure of the as-processed samples are summarized in Table 1. The dislocation density and the twin probability are two times higher for sample A in comparison with sample B. For a given technique used, TEM or XRD, it should be noticed that the grain/crystallite size values are the same within the experimental error for the two as-processed samples. In addition, the average grain sizes of both samples determined by TEM (by counting more than 200 grains) were about ~306 nm for sample A and ~318 nm for sample B. This is, in accordance with previous reports [37], three times larger than the size of the coherently diffracting domains measured by XRD profile analysis (~120 nm). The intensity ratio of NiO and Ni peaks at $2\Theta = 37.4^\circ$ and 44.6° indicates that the relative oxide content is slightly higher for sample A (0.6%) than for sample B (0.5%).

Fig. 2a shows a typical EBSD scan (presented is a part of a $100 \mu\text{m} \times 100 \mu\text{m}$ grid) of the as-processed microstructure in sample A and reveals that while no preferential grain orientation was found, the microstructure is heterogeneous and consists of a matrix of *ufg* grains within which micrometer-size (*mc*) grains are embedded. Some of these *mc* grains are subdivided into smaller grain blocks while still keeping more or less their initial spherical shape.

Table 1

The parameters of the microstructure obtained by TEM and X-ray line profile analysis. $I_{\text{NiO}}/I_{\text{Ni}}$ is the intensity ratio of the X-ray peaks for NiO and Ni at $2\theta = 37.5^\circ$ and 44° , respectively; ρ is the dislocation density and β is the twin-fault probability.

Sample	Grain size [nm] (TEM)	Crystallite size [nm] (XRD)	ρ [$\times 10^{14} \text{ m}^{-2}$]	$I_{\text{NiO}}/I_{\text{Ni}}$ [%]	β [%]
Sample A	306	121 ± 13	2 ± 0.2	0.6 ± 0.1	0.4 ± 0.05
Sample B	318	115 ± 12	1 ± 0.2	0.5 ± 0.1	0.2 ± 0.05

In both cases, the volume fraction of high angle grain boundaries (HAGBs) having misorientation higher than 15° was found to be about 85%. Thus, as expected from PM-process routes, the majority of the observed boundaries are HAGB. Another striking feature of the as-processed microstructures is the presence of a peak appearing at an angle of 60° in the misorientation distribution for sample A (Fig. 2b), whose presence is the characteristic of coherent $\Sigma 3$

boundaries such as twin boundaries (TBs) [29]. Indeed, the presence of these twin boundaries was confirmed by XRD analysis (reflected by the β parameter in Table 1) and by the TEM investigation as shown in Fig. 2c, for sample A. The twin thickness has been shown to follow a lognormal distribution as does the grain size [29] and not all grains were twinned. From the initial microstructure, it is concluded that the main microstructural differences between samples A and B are: the slightly smaller relative apparent mass density of sample A, and the two times higher densities of dislocations and twins for sample A compared to sample B.

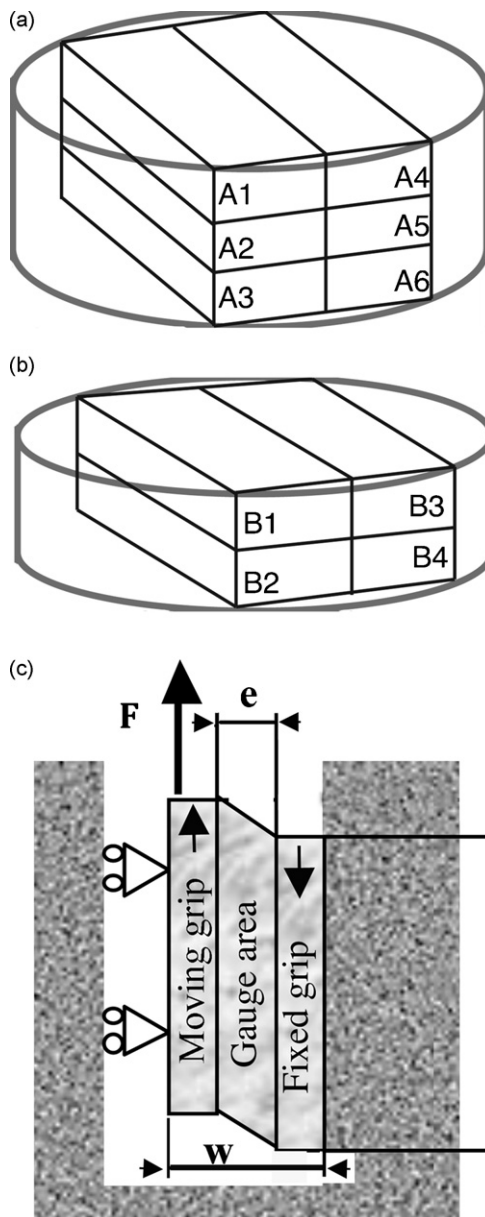


Fig. 1. Sketches of (a and b) the geometry and the location of the specimens within the disks. Letters A and B refer to the two as-processed disks and the numbers following the letters are associated with the mechanical tests (see text for details); (c) the shear device characteristics where L is the length (30 mm) and w is the width (18 mm) of the specimen; e is the width of the sheared region and F is the applied force. The vertical short arrows indicate the shear directions.

3.2. Mechanical properties

From the mechanical tests, the raw data obtained by simple shear tests represent the variation of the shear stress τ versus the amount of shear strain γ where:

$$\gamma = 2\varepsilon_{12} \quad \text{and} \quad \tau = \frac{F}{lh}, \quad (1)$$

F is the shearing force, while l and h denote the length and the thickness of the specimen, respectively, which are assumed to be constant during the simple shear test. The subscript 1 denotes the shearing direction and 2 the transverse direction. The value τ of the shear stress represents the average shear stress along the specimen. For comparison with data from literature, all the experimental curves obtained here are presented in terms of von Mises equivalent quantities (the shear strains and stresses are divided and multiplied by a factor equal to $\sqrt{3}$, respectively).

The characteristics of the main four mechanical tests were as follows:

- Monotonic simple shear test up to rupture, corresponding to an equivalent von Mises strain to the rupture of about $\varepsilon_{\text{VM}} = 0.125$.
- Cyclic load/unload simple shear test of a total of 5 cycles; the equivalent von Mises strains per cycle were about $\varepsilon_{\text{VM}} = 0.034$ and $\varepsilon_{\text{VM}} = 0.017$ for sample A and sample B, respectively. Therefore, the accumulated von Mises strains were $\varepsilon_{\text{VM}} = 0.17$ and $\varepsilon_{\text{VM}} = 0.09$, respectively.
- Bauschinger simple shear test of $\gamma_+ = 0.07$ in the forward direction and $\gamma_- = 0.30$ in the reverse direction. The accumulated von Mises strain was $\sim \varepsilon_{\text{VM}} = 0.20$.
- Cyclic Bauschinger simple shear test of 5 cycles of $\gamma_+ = 0.07$ in the forward direction and $\gamma_- = 0.07$ in the reverse direction. The accumulated von Mises strain was $\sim \varepsilon_{\text{VM}} = 0.75$.

3.2.1. The overall mechanical properties

The as-processed samples have shown some microstructure heterogeneities within the same compact (grain size, impurities and through-thickness variation of mass density). To illustrate the effect of such heterogeneities on the mechanical behavior, all the data of the shear tests conducted have been grouped on single diagrams displayed in Fig. 3a and b for samples A and B, respectively:

- For sample A, the stress-strain curves overlapped after Bauschinger (specimen A6 in Fig. 1a) and cyclic Bauschinger simple shear tests (specimen A4). The simple shear test (specimen A1) has apparently a higher flow stress and the behavior after simple shear load/unload test (specimen A5) was well below. Neverthe-

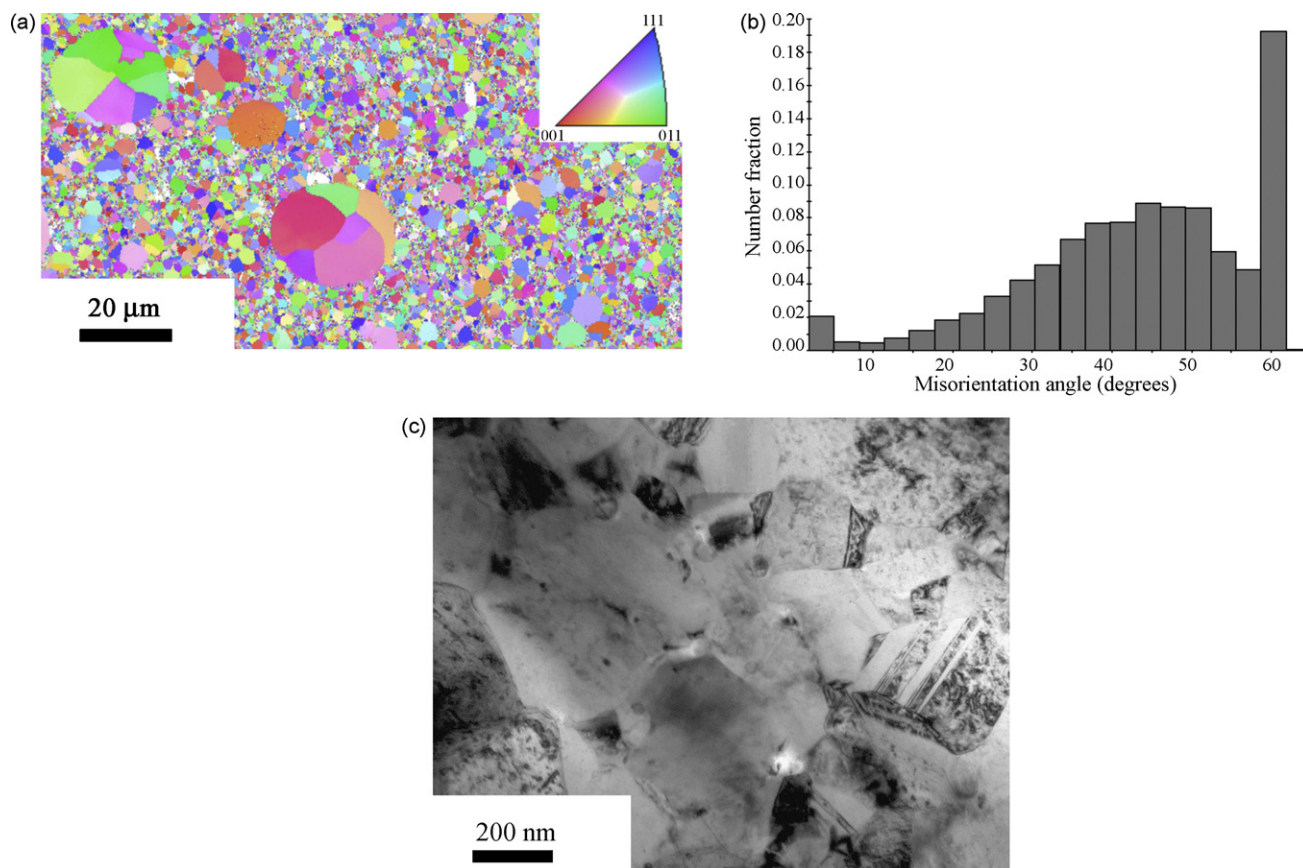


Fig. 2. Main characteristics of the as-processed microstructures for sample A. (a) Typical EBSD image of the microstructure; (b) the distribution of the misorientation angle across boundaries; (c) a TEM observation of the microstructure.

less, in another sequence of mechanical testing on sample A (not shown here) it was found that the stress–strain curves obtained in the monotonic simple shear test (specimen A3) and the first branch of the Bauschinger simple shear test (specimen A6) and that of the cyclic Bauschinger simple shear test overlapped.

- For sample B, the stress–strain curves of monotonic simple shear (specimen B2 in Fig. 1b) up to a strain of about $\varepsilon = 0.04$, Bauschinger (specimen B1) and cyclic Bauschinger simple shear (specimen B3) tests are nearly identical in their first branch. The cyclic load/unload simple shear curve (specimen B4) has a different evolution. It starts with a lower yield stress (200 MPa), but reaches more or less the same level of flow stress at higher strain.

Actually, the apparent discrepancies of the mechanical behavior within the same compact appear to be due to through-thickness microstructure heterogeneities. In particular, specimens extracted from the middle of the compact displayed poor mechanical properties. This is due to incomplete particle bonding (porosity). That was especially the case for specimens A2 and A5. Nevertheless, despite these drawbacks, the hardening capability and/or accumulated strain till rupture were better than that observed during compression test at room temperature of the same specimen [28,29]. The detailed comparison of the mechanical behavior of samples A and B for selected simple shear tests is now given below.

3.2.2. Monotonic simple shear tests

The stress–strain curves for monotonic simple shear tests are shown in Fig. 4a. The flow stress at an offset of 0.1% true plastic strain is about 715 MPa for sample A and 650 MPa for sample B. The reported flow stress at 0.1% offset strain is about 200 MPa for *cg* Ni

deformed in uniaxial tension at $\dot{\varepsilon} = 2 \times 10^{-3} \text{ s}^{-1}$ [38]. The equivalent von Mises plastic strain at rupture is about 0.12, about four times lower than *cg* counterpart (~ 0.4) [38]. The higher ductility of *cg* specimens compared to *ufg* samples may be attributed to the higher hardening capability of large grain-sized materials and the much lower amount of oxide phase as the oxide particles in the grain boundaries may cause weakening of boundary bonding in the compacted samples. Conversely, the ultimate von Mises equivalent stresses are of about 780 MPa and 730 MPa for samples A and B, respectively, which are much higher than the value, 280 MPa, characteristic for the *cg* counterpart [38]. It should be noted that sample A having a higher flow stress exhibits a lower ductility than sample B. This may be explained by both the slightly higher oxide content and the lower grain size of sample A.

In order to highlight the different strain-hardening regimes, Kocks–Mecking diagrams are plotted (Fig. 4b) where the strain hardening $\Theta = d\sigma/d\varepsilon$ is given against the stress σ . Initially the strain-hardening rate is extremely high at small plastic strains ($\Theta > \mu/10$, where μ is the shear modulus, 82 GPa for Ni). Then, it decreases rapidly and reaches a steady state at approximately $\Theta = \mu/200$. Similar behaviors were observed for both materials, with the exception that for sample A, a resuming of the strain hardening occurred in a burst-like manner as it spans a very narrow stress range. This burst can be attributed to the onset of a generalized plastic deformation that produces additional contribution of dislocation storage within the sample, which is absent or occurs in a limited extent in sample B. It can be also observed that the stress at which this burst occurs is slightly beyond the flow stress corresponding to 0.1% plastic deformation. As expected from Fig. 4a, the strain range of Θ_{III} hardening stage (i.e. parabolic hardening) is particularly short for both materials. This behavior has been recently observed

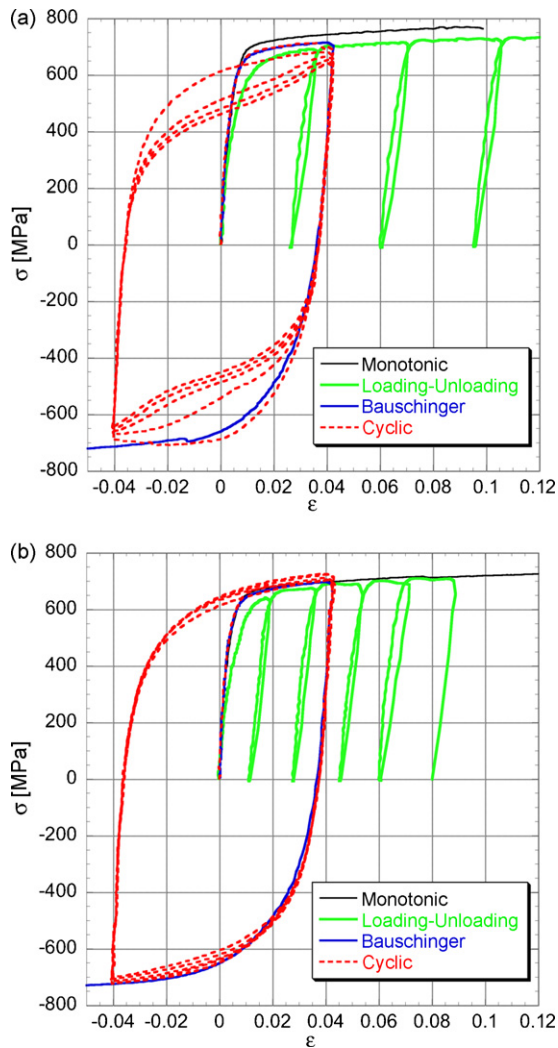


Fig. 3. The overall mechanical behavior following the various simple shear tests conducted on (a) sample A and (b) sample B.

in *ufg* (350 nm) Al–Mg alloy [39] and in *ufg* (400–500 nm) Cu [40].

3.2.3. Simple shear loading/unloading tests

Fig. 5a compares the mechanical behavior of the two materials when submitted to a simple shear test followed by subsequent unloading and reloading cycles. For sample A, the equivalent von Mises strain for each cycle was 0.035. This has led to a total equivalent von Mises strain before failure of about $\varepsilon = 0.17$, that is two times larger than in the case of monotonic simple shear test, for which the strain did not exceed $\varepsilon = 0.09$ before failure. As reported previously, the unloading/reloading stress–strain curves are highly non-linear with a non-negligible microplastic back/forward flow during unloading/reloading sequences. Nevertheless, the area of the “envelope” of the back/forward flow is by far smaller compared to that reported by Cosson [41] during cyclic simple shear tests of *ufg* Al processed by hot isostatic pressing (HIP) and having an average grain size of 120 nm. After unloading at an equivalent von Mises strain of about 6%, the short axis (full width at half maximum of the loops parallel to the strain axis) of back/forward loops corresponds to a strain $\Delta\varepsilon = 0.2\%$ for the Ni samples studied here while this value is $\sim 0.57\%$ for the *ufg* Al processed by HIP. In the latter case, the short axis of back/forward loops increases monotonously with increasing strain, while in the present investigation, the value of the short axis keeps constant from the beginning. Nevertheless, it is noticed that

when softening appears before unloading for the fourth unloading sequence of sample B (at $\varepsilon = 0.075$), more energy is dissipated (presence of damage), in accordance with Ref. [41]. Contrariwise, no backward strain was observed during loading/unloading tensile tests of *ufg* Cu [40]. Therefore, the observed back strain behavior seems to be a genuine effect of simple shear test. This point will be discussed in Section 5.

The details of the hardening evolution are displayed in Fig. 5b in terms of Θ – ε_{inc} curves, where $\varepsilon_{\text{inc}} = (\varepsilon^{\text{P}} - \varepsilon^{\text{pres}})$ with $\varepsilon^{\text{pres}}$ is the plastic prestrain and ε^{P} the plastic strain. The strain-hardening rates behavior for the two materials are quite similar. For the sake of clarity, only the hardening evolution of sample A is presented. The main characteristic here is the presence of a softening regime that occurs after the first unloading–reloading curve branch (area where Θ is negative), followed by a resuming of the hardening and then a steady state shows up, spanning a wide range of strains (see the second branch). This behavior is further exhibited by some amplifications and oscillations around $\Theta = 0$ at the beginning of the following cycles. This feature may be resulted from the back and forth dislocations motion due to the applied strain path.

3.2.4. Cyclic Bauschinger simple shear test

Fig. 6 illustrates the mechanical characteristics during cyclic Bauschinger simple shear test, which shows clearly different behaviors for samples A and B. Fig. 6a reveals that sample A exhibits

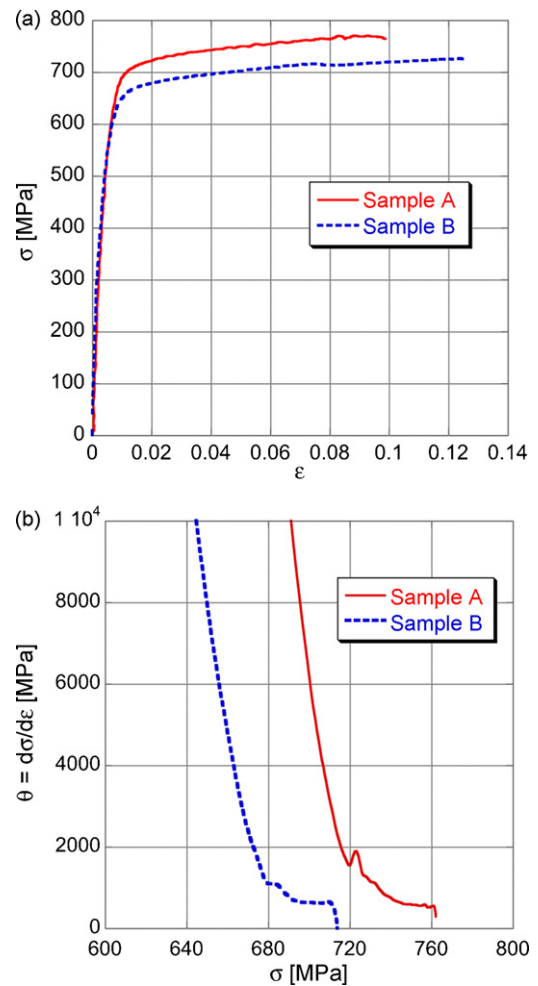


Fig. 4. The comparison of the mechanical behavior of sample A and sample B submitted to monotonic simple shear test at room temperature and at a strain rate of 10^{-3} s^{-1} (a) and the corresponding Kocks–Mecking plots (b). See the text for more details.

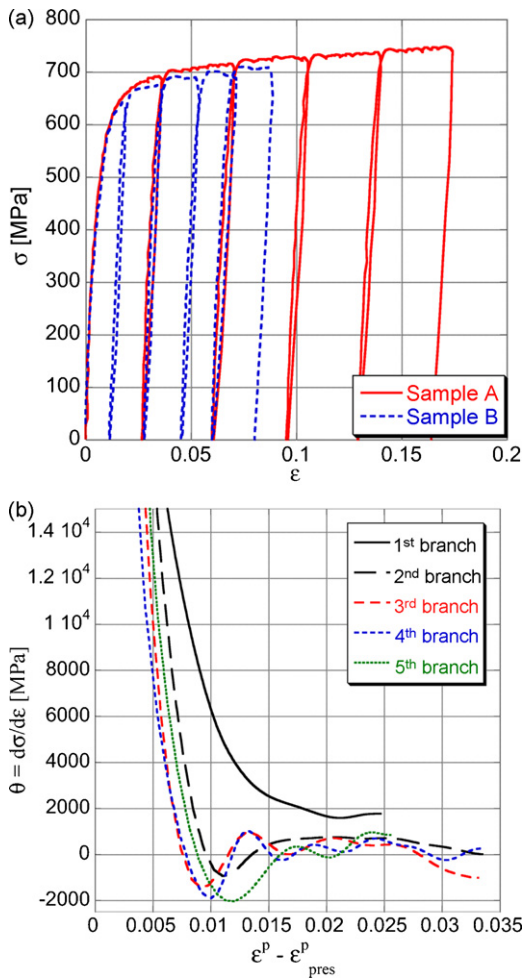


Fig. 5. Load/unload shear test conducted for samples A and B at room temperature and at a strain rate of 10^{-3} s^{-1} (a). The hardening behavior in each branch of the load/unload simple shear test for sample A (b).

stress softening during cycling (i.e. drop of the flow stress during cycling), with the occurrence of transitory strain-hardening regime (i.e. curve with rounded shape towards the interior of the loops). The flow stress at $\varepsilon = 0.04$ is about 700 MPa and drops down to 640 MPa for the last cycle at the same point in the curve. The softening rate is initially large and sets in between the first and the second cycles. Then, the scattering between the subsequent cycles diminished and the curves overlap reaching a quasi steady state. Despite the softening behavior, a tremendous accumulated strain before failure was observed. The computed deformation in terms of equivalent von Mises strain was about $\varepsilon_{VM} \approx 75\%$, far higher than observed in the case of the simple shear monotonic test.

The behavior of sample B strongly departs from that of sample A. Fig. 6b shows that the rate of stress softening is very low as indicated by the quasi-overlapping of the curves during cycling. In addition and contrary to sample A, a very small reduction of the maximum flow stress is observed during cycling. It dropped from about 730 MPa to 690 MPa between the first and the ultimate cycle, two times lower than in the case of sample A.

To further investigate the details of the hardening behavior, the “normalized” flow stress σ_i/σ_1 (where σ_i represents the absolute values of the flow stress at the end of the i th cycle in forward or reverse loading (at about $\varepsilon \cong 0.04$), and σ_1 is the flow stress value for the first loading cycle at $\varepsilon \cong 0.04$) for each sample has been plotted against the accumulated strain as shown in Fig. 6c. It is observed that the drop of the normalized flow stress is higher for sample A,

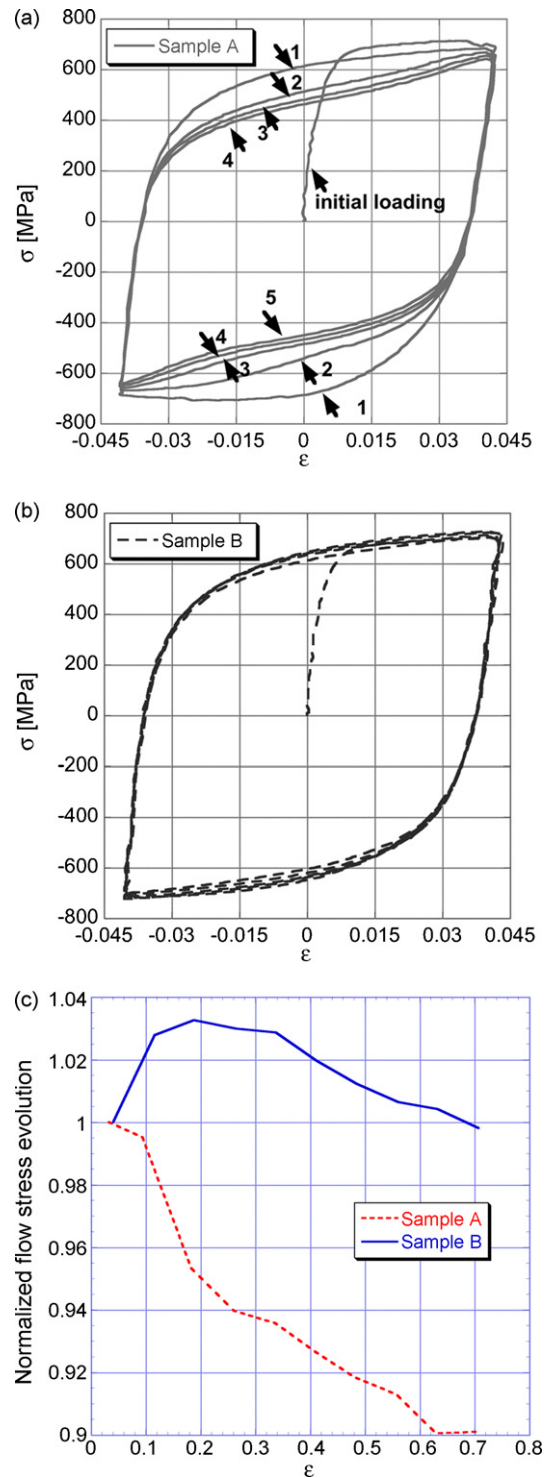


Fig. 6. Mechanical behavior during cyclic Bauschinger simple shear test at room temperature and at a strain rate of 10^{-3} s^{-1} for (a) sample A and (b) sample B. (c) Comparison of the softening evolution in terms of normalized flow stress against the accumulated strain.

particularly up to an accumulated strain of $\varepsilon \cong 0.2$, afterward the rate of softening is slowed down, reaching a quasi-static state after about $\varepsilon \cong 0.62$. Conversely sample B exhibited a hardening behavior during the first cycle of straining. This behavior is not clearly visible in Fig. 6b. After about $\varepsilon \cong 0.2$ a softening behavior is observed. The extent of the softening is very remote in comparison with sample A.

Table 2

The parameters of the microstructure obtained by X-ray line profile analysis. ρ is the dislocation density and β is the twin-fault probability.

Sample	Crystallite size [nm]	ρ [$\times 10^{14} \text{ m}^{-2}$]	β [%]
Sample A, after monotonic simple shear, $\varepsilon = 0.09$	68 \pm 7	11 \pm 1	0.2 \pm 0.05
Sample A, after cyclic Bauschinger test, $\varepsilon = 0.75$	104 \pm 11	12 \pm 1	0.2 \pm 0.05
Sample B, after monotonic simple shear, $\varepsilon = 0.12$	71 \pm 8	6 \pm 0.7	0.1 \pm 0.05
Sample B, after cyclic Bauschinger test, $\varepsilon = 0.75$	113 \pm 12	8 \pm 0.9	0.1 \pm 0.05

4. Microstructure characterization

4.1. XRD analysis of the deformed samples

Table 2 summarizes the microstructural parameters of the deformed samples after the simple shear and cyclic Bauschinger tests. The following evolution can be reported:

- The crystallite size decreased in the course of monotonic shear test for both samples. At the same time, the crystallite size remained unchanged within the experimental error during the cyclic Bauschinger simple shear tests. This may be due to the fact that the dislocations formed during cyclic testing are usually arranged into dipoles which cause negligible misorientation inside the grains. Therefore crystallites size reduction is expected to be very small after cyclic test contrary to the monotonic shear test. The stronger dipole character of dislocations for cyclically deformed samples was supported by the smaller value of the dislocation arrangement parameter (not shown here) determined by X-ray line profile analysis.
- The dislocation density (ρ) is about five to six times larger after shear tests than in the as-processed state for sample A. This holds true whatever the test method is, despite the amount of accumulated strain (0.75 for the cyclic Bauschinger simple shear test and 0.09 for the monotonic simple shear test). As for sample B, the dislocation density after straining is six and eight times higher (monotonic and cyclic Bauschinger tests, respectively) compared to that of the as-processed material.
- A decrease to about 50% of the twin probability, β (which is related to the twin density) is observed. This result is in accordance with a recent study by Gubicza et al. [29] that showed a dramatic decrease of the volume fraction of twin boundaries (TBs) during compression test of SPS and HIP processed bulk Ni materials.

4.2. TEM investigations of the deformed samples

Here we report only on some salient features of the microstructure that occurs during straining, in relation to what have been observed during XRD analysis. Therefore, only microstructure corresponding to monotonic and cyclic Bauschinger shear tests will be described here.

Fig. 7a illustrates an aspect of the microstructure of sample B deformed by monotonic simple shear up to rupture ($\varepsilon_{VM} = 0.12$). Two different behaviors of the TBs inside a micrometer-sized grain are observed. On the one hand, dislocations accumulate at the TBs (see the TBs at the bottom of the figure). Therefore these TBs act as obstacles to dislocations movement. On the other hand, TBs disentanglement (see the arrows at the top right) is observed as a consequence of strong interactions with lattice dislocations. In addition, it was also observed that some TBs become curved (not shown here) contrasting with the microstructure of the as-processed materials where TBs were straight.

Fig. 7b and c shows the microstructure characteristics of samples A and B after cyclic Bauschinger simple shear tests. The two micrographs are similar as they exhibit the same level of dislocation patterning which has led to dislocation of cells or subgrains, whose mean size is roughly about 200 nm, well below the initial

grain size, in direct line with XRD results. In addition the presence of TBs is scarce, except for some debris or residual contrasts that can be seen in Fig. 7b (see the black arrows). This paucity of TBs also contrasts with the observation made after a Bauschinger simple shear test (see Fig. 3), which can be considered as an intermediary stage of the cyclic Bauschinger simple shear test. In this case, the fraction of TBs is still high within the sample as shown in Fig. 7d, despite the fact that TBs interactions with gliding dislocations occur intensively (Fig. 7e). Therefore, it is suggested that the ultimate microstructure will mainly consist of cells or subgrains, with almost no TBs. This illustrates a sort of TBs “instability” in regard to shearing by lattice dislocations, as far as the materials studied here are concerned. This was, once again, confirmed by XRD profile analysis experiment.

5. Discussion

The majority of the mechanical tests carried out on *ufg* materials uses quasi-static uniaxial tensile or compression tests and indentation tests (microhardness or nanoindentation). As already mentioned, such mechanical tests indicate that the high strength is associated ineluctably in most cases, with limited ductility for uniaxial tension or with low failure strain for uniaxial compression.

In the present work, non-conventional mechanical characterization routes, using different simple shear loadings under finite strains were conducted to investigate the mechanical behavior of bulk ultrafine-grained Ni samples processed by SPS route. The investigated materials in the present work exhibit multi-level composite microstructure as indicated by SEM and TEM investigations. Indeed, the processed bulk materials have a significant volume fraction of micrometer-sized grains of about 15–20% (the largest grains are about 10 μm) embedded in a matrix of ultrafine grains. Besides, a small volume of NiO oxide phase was detected within the samples. The third characteristic of this composite microstructure was the presence of non-negligible fraction of grains (whatever their size) with growth-in twins, whose benefit on the mechanical behavior has been addressed in previous works [10,42–44]. Finally incomplete bonding during the SPS process has been found and results in through-thickness variation of amount of porosity. It is well known that porosity and impurities strongly impact on the mechanical behavior in conventional testing. In the present case, despite the observed stress softening (which may come from many sources), the behavior was quite different.

5.1. The monotonic shear behavior

After monotonic simple shear, the stress–strain curve (Fig. 4a) showed that a higher ultimate shear stress was achieved for sample A in comparison with sample B, and it was accompanied by a small uniform strain. This behavior may be, at the first place, explained by the oxide contents in the as-produced bulk materials, which could be sources of stress concentration during straining. Sample A has a higher content level of oxides. Therefore this sample hardens more, but fails at lower strain compared to sample B, probably as a consequence of grain boundaries cracking, as observed in [29] during compression test of the same specimens. Second, stress concentration may result from the tightening conditions of the samples. It has been observed [35] when grips with larger teeth are used, small

cracks occur at the surface of the strained sample. In the present study instead, finer grip teeth were adopted for both samples and the same torque was applied. Therefore the observed behavior is a genuine effect of the as-processed microstructures. The initial dislocation density of sample A was found to be twice that of sample

B, as was the twin probability. The higher density and twin probability for the as-processed sample A can be attributed to the two times longer processing time during SPS. It is assumed that during SPS-processing the consolidation mainly occurs by filling the voids between the particles by plastic flow of the material. The longer

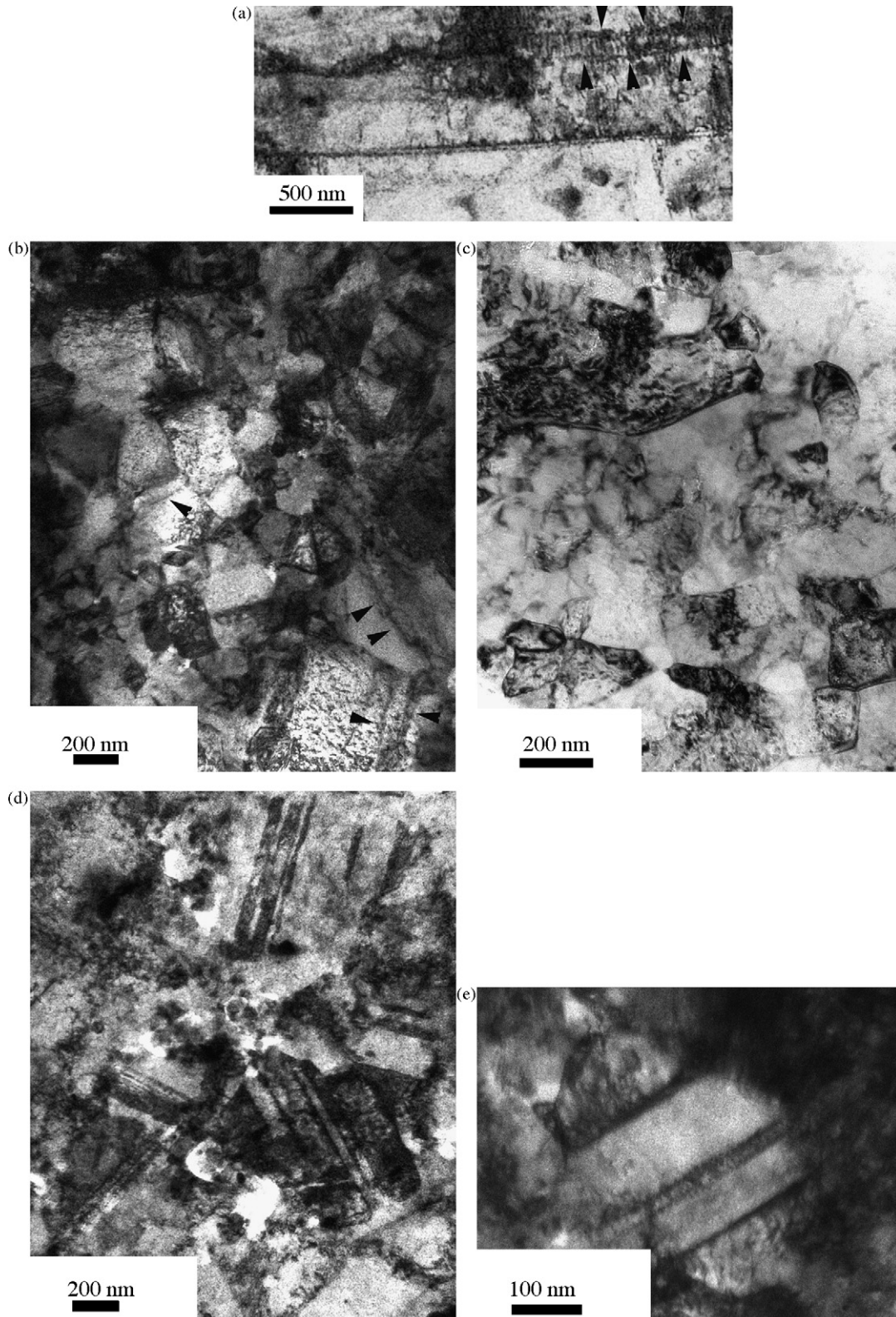


Fig. 7. Typical microstructures of the samples deformed till rupture. (a) After simple shear test for sample B; (b) after Bauschinger cyclic simple shear for sample A; (c) after Bauschinger cyclic simple shear for sample B; (d) after Bauschinger simple shear for sample B; (e) after Bauschinger cyclic simple shear for sample B.

the time of consolidation, the higher the density of lattice defects formed during plastic deformation taking place in SPS-processing. The two times higher initial densities of lattice defects for sample A may explain partially the higher flow stress during monotonic shear test and the higher dislocation density and twin probability observed after the shearing of sample A.

Further, one main difference between the mechanical behaviors of samples A and B is the burst observed in the strain-hardening rate evolution of sample A, which corresponded to the onset of plastic deformation producing more dislocations, whose storage and subsequent interaction with TBs and general grain boundaries may lead to the observed hardening behavior. Therefore, it seems that the subsequent behavior strongly depends on the amount of dislocations produced at the onset of plastic deformation.

5.2. The cyclic shear behavior

5.2.1. The work-hardening behavior

Cosson [41] conducted cyclic simple shear tests on conventional O-state AA5182 aluminum alloy and on pure *ufg* Al processed by HIP. They observed that the area of the unloading–reloading loops increases with the accumulated shear strain, contrariwise to the behavior of the *cg* 5182 alloy. The authors attributed this effect to energy dissipation related to grain boundary deformation mechanisms. In addition, it was found that the slope of the curve decreased during straining. This effect was attributed to intergranular damage accumulation, leading ultimately to grain boundaries fracture. In the present case, the slopes of the unloading curves as well as the “envelope” of the unloading/reloading loops remain constant for the different cycles, in accordance with the behavior of *cg* Al [40] or that of ECAP-processed *ufg* Al [12]. In the latter case, this behavior was ascribed to either high level of internal strain or dislocation interactions with grains boundaries [12]. Therefore, because of the lognormal grain size distribution, it is probable that grain boundary-related deformation mechanisms may be also involved here.

Strain hardening and softening behaviors have been reported during cyclic shear tests of *cg* AA 3004 and AA 5182 aluminum alloys [45,46]. For instance, in the case of AA 3004 alloy, a dramatic softening has been reported for alloys in the extra-hardened H19 metallurgical state. It was shown that softening occurred by the way of a large-scale microstructural reorganization via microbands formation. Contrariwise, for the alloy in the O-state, the samples exhibited strain hardening that was accompanied by dislocation cells and subgrains formation of smaller size and increased misorientations [46]. In the case of AA 5182 alloys, whatever the state, a work-hardening behavior was reported during the first cycle. The subsequent increase of the flow stress was very small and the deformation ended up with a saturation cycle. Planar dislocation patterning was observed, instead of dislocation cells, due to the dislocation interactions with Mg solute atoms. In the present case, a non-negligible fraction of twin has been revealed by TEM and XRD investigations, along with oxides dispersion within the *ufg* matrix. In both samples, cyclic softening has been observed, whose intensity was low for sample B. Therefore, the role of the oxide dispersion on the cyclic hardening behavior is very small compared to the dislocation locking effect of Mg solute atoms. It has been reported that twin boundaries may act as general boundaries, i.e. obstacles to plastic deformation [47]. In other reports, twin boundaries disentanglement has been reported during straining of *ufg* Ni processed by PM routes [28,29], which has been also confirmed here. Therefore it is suggested that TBs instability in regard to the imposed plastic deformation may weaken the microstructure and contribute to the softening behavior, whose intensity may depend on the initial twin density, their distribution and their relative orientation to the shear direction. The observed resuming of hardening

after strain reversal for sample A may be attributed not only to a local dislocation density increase provided by the disrupted TBs, but also to formation of dislocation locks such as Lomer–Cottrell junctions in the course of deformation. However, it should be noted that the lower relative density of sample A may also contribute to the softening during cyclic Bauschinger test. The lower relative density may be at least partially caused by the higher porosity of the sample as this specimen was prepared from the middle of the sintered disk. The higher porosity may cause microcracking during the first cycle of the test which can result in lower flow stress in the subsequent cycles. Furthermore, the higher total oxide content in sample A probably involves higher oxide content on the grain boundaries which may reduce the grain boundary strength resulting in an easier cracking during deformation and softening in the cyclic Bauschinger test. In total, the effect of porosity and the reduced grain boundary strength in sample A explain the slightly lower flow stress for sample A after the cyclic Bauschinger test in spite of the higher densities of dislocations and twins compared to sample B (see Table 2).

5.2.2. The internal stresses

Cyclic shear tests allowed to estimate the level of the internal stresses during straining. To this end, the flow stress at the end of the first branch σ^+ and the beginning of the second branch σ^- of the stress–strain curves (without the elastic part) are determined. Absolute and relative kinematic work-hardening (denoted by X and X_{rel} , respectively) at $\varepsilon \approx 4\%$ are calculated using the relations:

$$X = \frac{\sigma^+ - \sigma^-}{2}; \quad X_{rel} = \frac{X}{\sigma^+}.$$

The computed values were $(X, X_{rel}) = (216 \text{ MPa}, 30\%)$ for sample A, and $(X, X_{rel}) = (180 \text{ MPa}, 26\%)$ for sample B. These values are of the same order of magnitude as those found in coarse-grained dual phase steels. In this case, a volume fraction of about 10% of a hard martensite phase embedded in soft ferritic matrix resulted in high internal stresses due to the strain incompatibility between these phases [35]. In the present case, the higher volume fraction of grain boundaries due to the *ufg* microstructure, along with TBs and the presence of the oxide phase may contribute to the building of such high level of internal stresses.

6. Conclusions

The mechanical behavior of bulk *ufg* Ni samples processed by SPS of a high purity nanopowder has been investigated by non-conventional mechanical testing, that consisted of shear tests of large strain amplitude. Despite the low level of relative mass density and inhomogeneous initial microstructure, it is shown that, contrariwise to the limited room temperature deformation capability of the majority of *ufg* materials under quasi-static monotonic straining conditions, the shear tests, particularly cyclic shear tests, resulted in a high amount of accumulated deformation, combined with an acceptable level of the flow stress.

The high level of accumulated deformation allowed uncovering some specific features of *ufg* materials, especially those processed by PM routes. The role of annealing twins has been stressed. On the one hand and up to a certain deformation level, TBs acted as obstacles to dislocations as do general grain boundaries and maintain a certain amount of hardening during monotonic straining. On the other hand and contrariwise to what is usually reported in the literature, for samples studied here, twin boundaries appeared to be instable during shear tests. Particularly, during cyclic shearing it was found that the TBs instability induces work softening whose intensity depends, of course, on the initial twins density. The porosity and the grain boundary strength may also contribute to the softening during cyclic test.

Acknowledgements

JG is grateful for the support of a Bolyai Janos Research Scholarship of the Hungarian Academy of Sciences. G. Dirras is very grateful to Dr. H.Q. Bui for TEM investigations.

References

- [1] S. Billard, J.P. Fondere, B. Bacroix, G.F. Dirras, *Acta Mater.* 54 (2006) 411–421.
- [2] W.Q. Cao, G.F. Dirras, M. Benyoucef, B. Bacroix, *Mater. Sci. Eng. A* 462 (2007) 100–105.
- [3] E.O. Hall, *Proc. Phys. Soc. B-64* (1951) 747.
- [4] N.J. Petch, *J. Iron Steel Inst.* 174 (1953) 25–28.
- [5] K.S. Kumar, S. Suresh, M.F. Chisholm, J.A. Horton, P.J. Wang, *Acta Mater.* 51 (2003) 387–405.
- [6] M.A. Meyers, A. Mishra, D.J. Benson, *Prog. Mater. Sci.* 51 (2006) 427–556.
- [7] S.G. Tjong, H. Chen, *Mater. Sci. Eng. R* 45 (2004) 1–88.
- [8] M. Chen, E. Ma, K.J. Hemker, in: G.I. Gogotsi (Ed.), *Handbook of Nanomaterials*, CRC Press, 2006, pp. 497–529.
- [9] A.A. Karimpoor, U. Erb, K.T. Aust, G. Palumbo, *Scripta Mater.* 49 (2003) 651–656.
- [10] M. Dao, L. Lu, Y.F. Shen, S. Suresh, *Acta Mater.* 54 (2006) 5421–5432.
- [11] Y.M. Wang, E.J. Ma, *Acta Mater.* 52 (2004) 1699–1709.
- [12] H. Mughrabi, H.W. Höppel, M.J. Kautz, *Scripta Mater.* 51 (2004) 807–812.
- [13] H.W. Höppel, M. Kautz, C. Xu, M. Murashkin, T.G. Langdon, R.Z. Valiev, H.J. Mughrabi, *Int. J. Fatigue* 28 (2006) 1001–1010.
- [14] A.Y. Vinogradov, V.V. Stolyarov, S. Hashimoto, R.Z. Valiev, *Mater. Sci. Eng. A* 318 (2001) 163–173.
- [15] H.J. Maier, P. Gabor, N. Gupta, I. Karaman, M.J. Haouaoui, *Int. J. Fatigue* 28 (2006) 243–250.
- [16] S.R. Agnew, J.R. Weertman, *Mater. Sci. Eng. A* 244 (1998) 145–153.
- [17] M. Haouaoui, I. Karaman, H.J. Maier, K.T. Hartwig, *Metall. Mater. Trans. A* 35 (2004) 2935–2949.
- [18] J. Aktaa, J. Reszat, M. Walter, K. Bade, K.J. Hemker, *Scripta Mater.* 52 (2005) 1217–1221.
- [19] S. Brandstetter, Deformation mechanisms of nanocrystalline nickel studied by in-situ X-ray diffraction, PhD Thesis, EPFL, Lausanne, 2008.
- [20] S. Brandstetter, K. Zhang, A. Escudro, J.R. Weertman, H. Van Swygenhoven, *Scripta Mater.* 58 (2008) 61–64.
- [21] Z. Budrovic, H. Van Swygenhoven, P.M. Derlet, S. Van Petegem, B. Schmitt, *Science* 304 (2004) 273–276.
- [22] Y.-Y. Chao, S.K. Varma, *Scripta Metall. Mater.* 24 (1990) 1665–1668.
- [23] F. Dalla Torre, P. Spatig, R. Schaublin, M.J. Victoria, *Acta Mater.* 53 (2005) 2337–2339.
- [24] K.J. Hemker, H.J. Last, *Mater. Sci. Eng. A* 319–321 (2001) 882–886.
- [25] R. Schwaiger, B. Moser, M. Dao, N. Chollacoop, S.J. Suresh, *Acta Mater.* 51 (2003) 5159–5172.
- [26] T.E. Buchheit, D.A. LaVan, J.R. Michael, S.D. Leith, *Metall. Mater. Trans.* 33A (2002) 539–554.
- [27] H.S. Cho, K.J. Hemker, K. Lian, J. Goettter, G. Dirras, *Sens. Actuators A* 103 (2003) 59–63.
- [28] H.Q. Bui, PhD Thesis, University of Paris 13, Villetaneuse, 2008.
- [29] J. Gubicza, H.Q. Bui, F. Fellah, G.F. Dirras, *J. Mater. Res.* 24 (2009) 217–226.
- [30] Y.-S. Kwon, Y.-H. Jung, N.A. Yavorovsky, A.P. Illyin, J.-S.J. Kim, *Scripta Mater.* 44 (2001) 2247–2251.
- [31] F. Tepper, *Met. Powder Rep.* 53 (1998) 31.
- [32] S. Paris, E. Gaffet, F. Bernard, Z.A. Munir, *Scripta Mater.* 50 (2004) 691–696.
- [33] G. Ribarik, J. Gubicza, T. Ungar, *Mater. Sci. Eng. A* 387–389 (2004) 343–347.
- [34] L. Balogh, G. Ribarik, T. Ungar, *J. Appl. Phys.* 100 (2006) 023512.
- [35] S. Bouvier, H. Haddadi, P. Levee, C. Teodosiu, *J. Mater. Process. Technol.* 172 (2006) 96–103.
- [36] S. Bouvier, B. Gardey, H. Haddadi, C. Teodosiu, *J. Mater. Process. Technol.* 174 (2006) 115–126.
- [37] A.P. Zhilyaev, B.K. Kim, J.A. Szpunar, M.D. Baro, T.G. Langdon, *Mater. Sci. Eng. A* 391 (2005) 377–389.
- [38] N. Krasilnikov, W. Lojkowski, Z. Pakiela, R. Valiev, *Mater. Sci. Eng. A* 397 (2005) 330–337.
- [39] O. Nijs, B. Holmedal, J. Friis, E. Nes, *Mater. Sci. Eng. A* 483–484 (2008) 51–53.
- [40] X.H. Chen, L. Lu, *Scripta Mater.* 57 (2007) 133–136.
- [41] B. Cosson, Master Thesis, University of Paris 13, Villetaneuse, 2005.
- [42] L. Lu, R. Schwaiger, Z. Shan, M. Dao, K. Lu, S. Suresh, *Acta Mater.* 33 (2005) 2169–2179.
- [43] Y.F. Shen, L. Lu, M. Dao, S.J. Suresh, *Scripta Mater.* 55 (2006) 319–322.
- [44] X.H. Chen, L.J. Lu, *Scripta Mater.* 57 (2007) 133–136.
- [45] G.F. Dirras, *Mater. Sci. Eng. A* 234–236 (1997) 966–969.
- [46] G.F. Dirras, J.-L. Duval, W. Swiatnicki, *Mater. Sci. Eng. A* 263 (1999) 85–95.
- [47] L. Lu, X. Chen, X. Huang, K. Lu, *Science* 323 (2009) 607–610.